Direct Determination of Polarity, Faceting, and Core Location in Colloidal Core/Shell Wurtzite Semiconductor Nanocrystals

Giovanni Bertoni,[†,‡,*] Vincenzo Grillo,[†,§] Rosaria Brescia,[‡] Xiaoxing Ke,[⊥] Sara Bals,[⊥] Alessandra Catellani,[†] Hongbo Li,[‡] and Liberato Manna[‡,*]

[†]IMEM-CNR, Parco Area delle Scienze 37/A, IT 43124 Parma, Italy, [‡]Istituto Italiano di Tecnologia, Via Morego 30, IT 16163 Genova, Italy, [§]S3-CNRNANO, Via Campi 213/A, IT 41125 Modena, Italy, and [⊥]EMAT, University of Antwerp, Groenenborgerlaan 171, BE 2020 Antwerp, Belgium

ABSTRACT The ability to determine the atomic arrangement and termination of various facets of surfactant-coated nanocrystals is of great importance for understanding their growth mechanism and their surface properties and represents a critical piece of information that can be coupled to other experimental techniques and to calculations. This is especially appealing in the study of nanocrystals that can be grown in strongly anisotropic shapes, for which the relative growth rates of various facets can be influenced under varying reaction conditions. Here we show that in two representative cases of rod-shaped nanocrystals in the wurtzite phase (CdSe(core)/CdS(shell) and ZnSe(core)/ZnS(shell) nanorods) the terminations of the polar facets can be resolved unambiguously by combining advanced electron microscopy techniques, such as aberration-corrected HRTEM with exit wave reconstruction or aberration-corrected HAADF-STEM. The [0001] and [000−1] polar directions of these rods, which grow preferentially along their *c*-axis, are revealed clearly, with one side consisting of the Cd (or Zn)-terminated (0001) facet and the other side with a pronounced faceting due to Cd (or Zn)-terminated {10−1−1} facets. The lateral faceting of the rods is instead dominated by three nonpolar {10−10} facets. The core buried in the nanostructure can be localized in both the exit wave phase and HAADF-STEM images.

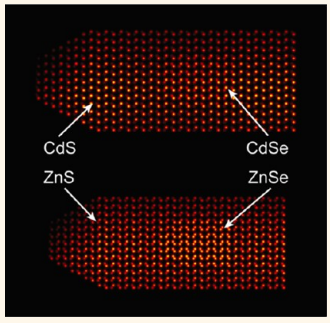

KEYWORDS: polarity · wurtzite · nanocrystals · HRTEM · HAADF-STEM · exit wave reconstruction

The experimental determination of crystal termination in nanostructures is not an easy task in conventional transmission electron microscopy, since only an aberrated two-dimensional projection of the structure can be directly imaged in the microscope.[1] In non-centrosymmetric crystals, *i.e.*, polar crystals (which have no inversion symmetry), intermediate steps in the characterization of the crystal polarity[2] and the object morphology are required, which are both not trivial. A polar crystal slab ends with opposite atomic surfaces having different chemical reactivities[3] or different electronic behavior in the contacts.[4] Therefore the determination of crystal polarity actually has fundamental and technological implications, especially for the integration of these nanostructures as building blocks in electronic and photonic devices. In the case of epitaxially grown extended structures, it is well established that the orientation (and thus the polarity) of the grown structure is dictated by the (known) crystallographic orientation of the substrate.[5] Experimental techniques such as transmission electron microscopy (TEM) and especially convergent beam electron diffraction (CBED)[2,6] or X-ray photoelectron diffraction (XPD)[7] can be used to solve the polarity termination of bulk extended structures, but in the case of nanostructures these techniques are of more difficult application. This is very unfortunate, since the information on polarity could be exploited for clarifying issues such as the growth mechanism of nanostructures and their surface properties, and in addition it could be coupled to other experimental techniques and to modeling.

One popular example of nanostructures is represented by colloidal nanocrystals of II−VI semiconductors in the hexagonal wurtzite structure.[8−14] These nanocrystals can be easily grown in shapes that are elongated along their polar *c*-axis or even in branched shapes consisting of various elongated domains connected at branching points, and recently also in nanosheets, by using specific surfactant molecules and synthesis conditions.[13,15−17] Techniques such as nuclear magnetic resonance (NMR) and Fourier transform infrared

* Address correspondence to giovanni.bertoni@imem.cnr.it; liberato.manna@iit.it.

Received for review May 11, 2012 and accepted June 18, 2012.

Published online June 18, 2012
10.1021/nn302085t

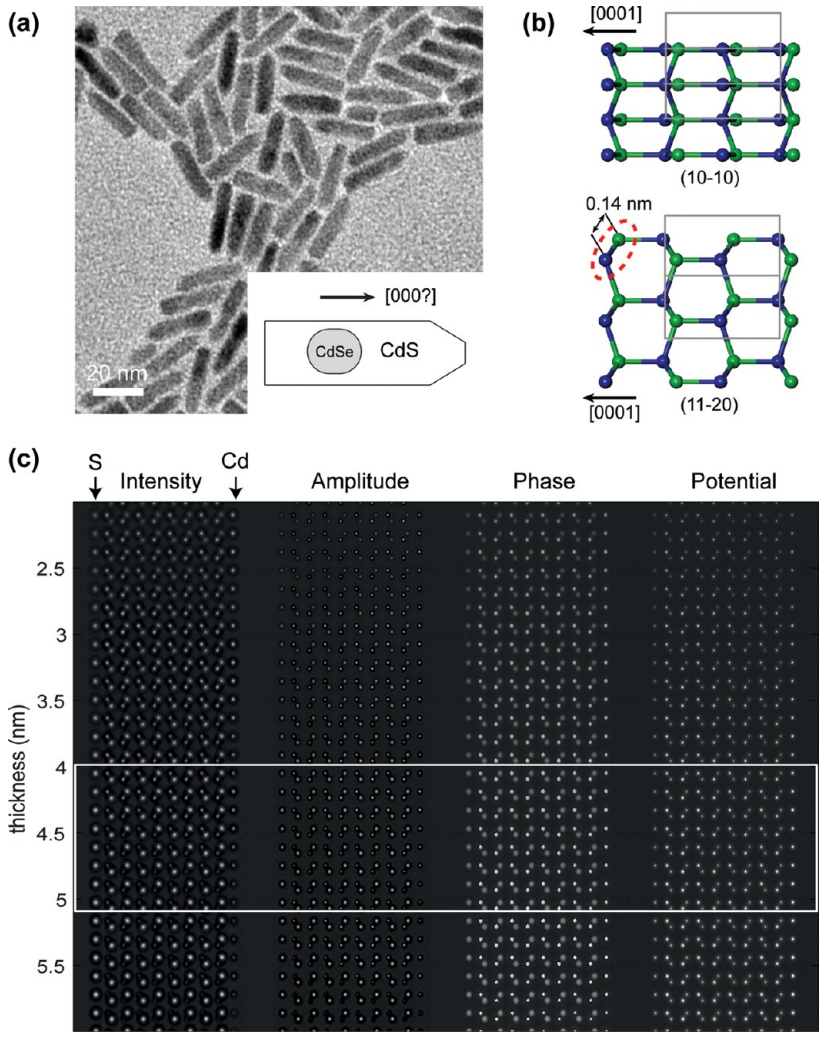

Figure 1. (a) Low-magnification bright field TEM view of a group of CdSe/CdS nanorods. The inset shows a sketch of the particle structure as it is known from the literature. (b) Top views of the wurtzite structure for CdS, facing the (10−10) and (11−20) surfaces. The cation (Cd) is blue, and the anion (S) is green. The cations have one bond toward the [0001] direction and three toward the [000−1] direction. When seen along the [11−20] direction, the Cd−S dumbbell (indicated by the dashed circle) has a projected separation of about 0.14 nm. (c) Simulated image intensity (at the conditions described in Table T1 of the Supporting Information) and EW amplitude and phase, together with the projected potential, as a function of thickness for a CdS wedge (from 2 to 6 nm thick) oriented along the [11−20] zone axis. The image intensity and EW amplitude show contrast transfer at about 4 nm thickness (see the marked area in the image) from Cd toward S due to amplitude channeling, complicating a direct assignment of the atoms in the HRTEM image, while the EW phase still stays peaked on Cd atoms, as expected from the potential image.

(FT-IR) spectroscopy can be used to identify the stabilizing agents that actually bind strongly to the surface of nanocrystals and therefore influence their growth. This information, in combination with simple considerations of surface energy, with calculations,[18−25] and with the experimental evidence of the different morphologies obtained by growth under various reaction conditions,[26] may help to make reasonable conclusions on facet polarities.

In nanorods of II−VI semiconductors, for example, much can be guessed from the type of surfactants used to control the growth of the nanocrystals.[19,20] These surfactants bind preferentially to the metallic atom (*e.g.*, Cd or Zn), so that the polar facets, *i.e.*, those facets that expose only one type of atom (either cations or anions), should be terminated preferentially by the metallic atom, that is the cation. In addition to that, polar facets in which the metallic species expose too many dangling bonds should be unstable and tend to be replaced by other facets, which could be either nonpolar facets or even other higher index polar facets with metallic atoms exposing a lower number of dangling bonds. The differences in chemical reactivities between the polar terminations in nanocrystals of II−VI semiconductors have been exploited also in the growth of either a metal domain (most often Au) or a semiconductor domain at one tip of the nanorods.[27−31] Studies on the oriented attachment of CdS nanorods are in agreement with the presence of two opposite polar terminations with respect to the *c*-axis, with different chemical reactivities.[32] Another example is represented by colloidal wurtzite core/shell CdSe/CdS nanorods consisting of an approximately

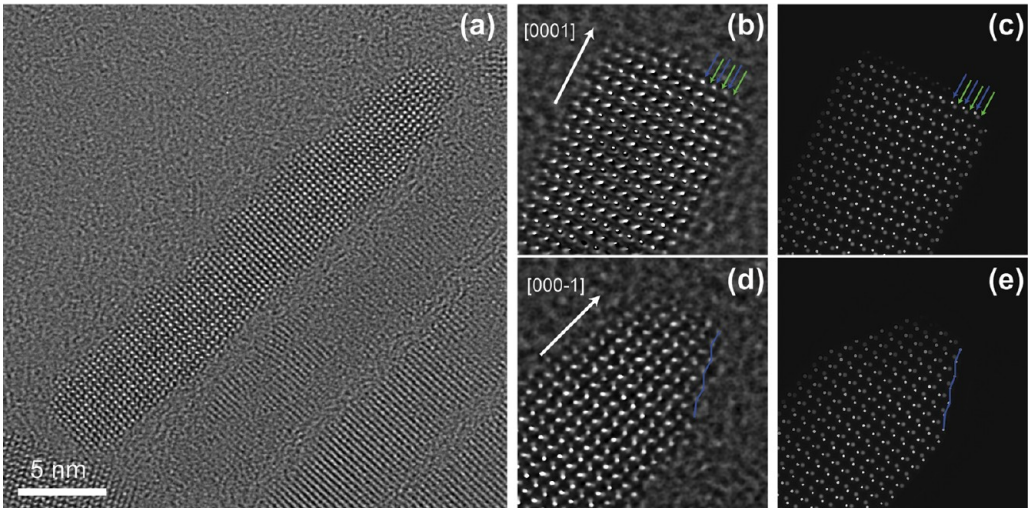

Figure 2. (a) View of a CdSe/CdS rod along the [11−20] zone axis, from a single HRTEM image of the focal series, with resolved Cd−S dumbbells, appearing bright as expected in NCSI conditions. From single HRTEM images, it is hard to distinguish Cd columns from S columns. (b, d) Experimental and (c, e) simulated EW phase from the set of 20 images of the two ends of the nanorod. The bright spots of the dumbbells in the phase correspond to Cd atoms, according to Figure 1c. The flat side of the rod (b, c) can then be addressed as the [0001] polar side, exposing Cd atoms, while the tip (d, e) is oriented toward the [000−1] direction. The blue lines follow the Cd atoms at the edge of a (10−1−1) facet.

spherical CdSe core encased in a thick, rod-shaped CdS shell (Figure 1a).[33−35] These rods often have a flat termination on one side and a sharpened tip on the opposite side, with respect to their elongation direction, again along the *c*-axis (see sketch in Figure 1a). Also, it was found that the CdSe core is often located toward one side of the nanorod and not really at its center (this localization was possible both by strain analysis techniques based on lattice spacing variations[34,36] and by the ionization signal of the Se in the core).[36,37] The asymmetric location of the core indicates that the rods grow faster in one polar direction along the *c*-axis than in the opposite one (see inset in Figure 1a).

All the studies discussed above clearly pointed to a difference in reactivity between the polar terminations of wurtzite nanocrystals and in the growth rates along the opposite directions of their *c*-axis.[37] A direct separation of the [0001] and the [000−1] directions was given by McBride *et al.*[38] and by Rosenthal *et al.*[39] *via* ultrahigh resolution in the TEM, by means of spherical aberration correction in the scanning mode (high-angle annular dark field (HAADF)-STEM),[40,41] so as to resolve the cation−anion *dumbbells* in the structure (see the sketches in Figure 1b).

In the present work, we report an experimental identification of the polarity in rod-shaped wurtzite nanocrystals (Figure 1a) by direct imaging in the TEM, not only in scanning mode (HAADF-STEM) but also in imaging mode (HRTEM).[42] In HRTEM we retrieve the complex wave function after the electrons have traveled through the sample (called the *exit wave*, or EW) to separate amplitude and phase and address the two atomic columns in the dumbbell. In this way it is possible to distinguish between the [0001] and the [000−1] directions along the *c*-axis also in HRTEM, such that the terminations of the two opposite polar surfaces can be seen. Besides the information on polarity, other important features can be derived, for example, which surfaces are forming the lateral facets of the nanorods and whether some atomic columns are missing at their edges. From multiple projections of the same nanocrystal, a model for the 3D structure can be proposed. This permits us to identify dominant lateral or tip facets. Additionally, the location of the core in core/shell nanorods can be extracted from both EW and HAADF-STEM.

RESULTS AND DISCUSSION

Determination of the Polarity. Figure 1c shows the results of a HRTEM simulation on a CdS wedge of increasing thickness. Despite that Cd atoms ($Z = 48$) are heavier than S atoms ($Z = 16$), the condition of weak phase object approximation is not fulfilled, except at very low thicknesses, and the recorded image is a mixture of amplitude and phase contrast,[43] with the contrast in the image affected by the amplitude transfer from Cd to S columns. This depends on the extinction distance, *i.e.*, the distance along *z* over which the wave amplitude is transferred back and forth once on a column and which is different for Cd and S columns (being shorter for Cd).[1] As a result, at 4 nm thickness the intensity from the S column atoms reaches the intensity of the Cd column atoms, and it becomes dominant at higher thicknesses, making the interpretation of the acquired image nontrivial. The procedure to extract the phase factor and to remove constant factors is based on the channeling theory and is explained in the Methods section.[44] As a result, the calculated phase is peaked on the Cd atoms also at higher thicknesses, giving a direct interpretation of the structure in terms of the projected potential. This demonstrates that the retrieval of the object EW phase

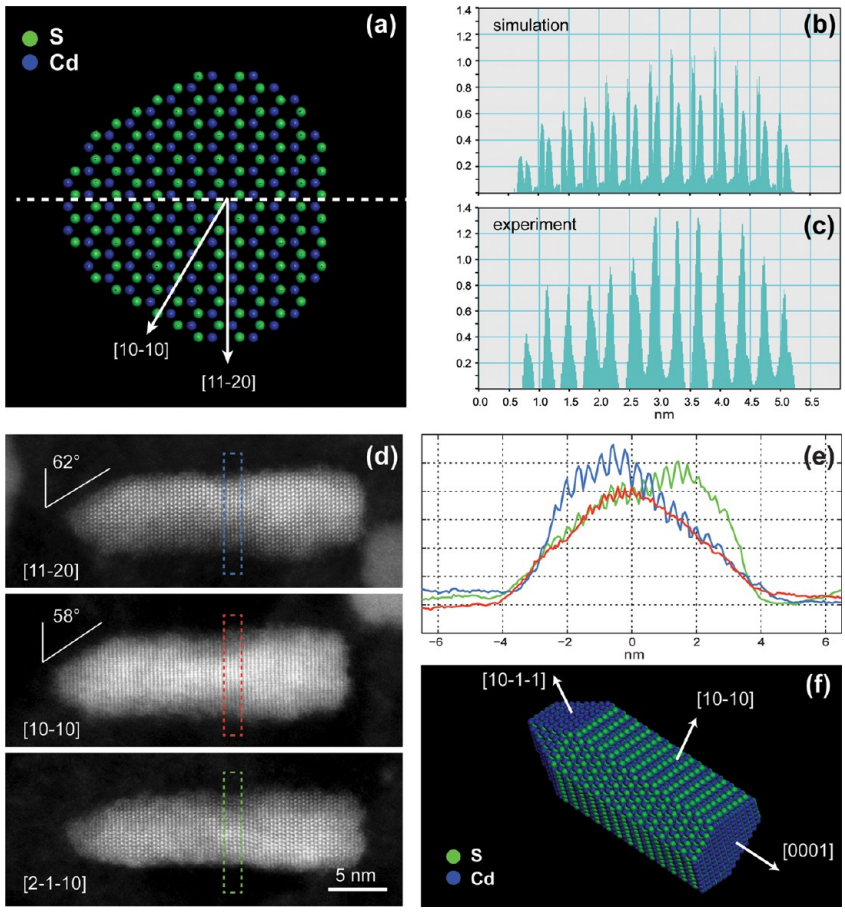

Figure 3. (a) Cross-section view of a Cd−S layer from the rod model in (f) used for simulations (with dominant {10−10} facets). (b, c) Integrated profiles of the EW phase from the simulation and the experiment, both with an asymmetry as expected from the thickness profile along the dashed line in (a). (d) Faceting of a CdSe/CdS rod from HAADF-STEM projections. (e) The integrated profile is symmetric in the [10−10] orientation, while it is asymmetric in the [11−20] and [2−1−10] projections, confirming that the nonpolar side facets developed during growth are indeed {10−10}.

is then necessary to unambiguously address the two atoms in the dumbbells by HRTEM. The phase of the EW can be used to probe the thickness and compositional change at atomic scale in the [11−20] projections (where the dumbbells can be clearly resolved; see Figure 1b). Moreover, the contrast in the EW phase has approximately linear dependence on the atomic number *Z*, being suitable to enhance the contribution of light elements such as sulfur.

As a complementary quantitative technique we used HAADF-STEM, working on a FEI Titan^3 50-80 microscope equipped with both image and probe correctors and working at 120 or 300 kV. This technique has been mainly exploited to solve the lateral faceting of the nanorods, making use of three projections ([2−1−10], [10−10], and [11−20]) from the same rod. The dynamical propagation has a lower effect on the HAADF-STEM images, where the intensity can be considered approximately incoherent and proportional to the square of the atomic number (Z^2),[45] giving a more directly interpretable measurement of a single image, but enhancing the contrast for heavier elements. The two techniques (as will be shown further in the text) gave consistent results.

In Figure 2a a CdSe/CdS rod is displayed. The imaging conditions of imaging are close to the optimal calculated values (see Table T1 in the Supporting Information). The Cd−S projected dumbbells show a bright contrast, as expected from the imaging conditions at negative spherical aberration (NCSI).[43] To reduce the delocalization[46] and to discriminate between Cd and S atomic columns as explained above, we retrieved the EW phase. The results are presented in Figure 2b,c for the flat tip of the rod. First, the orientation of the dumbbells reveals that the flat tip of the rod is formed in the [0001] direction. The faceted tip of the rod should then be in the [000−1] direction, as revealed clearly in Figure 2d,e (see also Figure S2c,d in the Supporting Information).

Our findings agree with the previous HAADF-STEM results on CdSe-based core/shell nanocrystals[39] and represent a further experimental proof of the hypothesis formulated in many works.[13,14,47] They are indeed consistent with the dangling bonds arguments discussed in the introduction. For example it has been shown that the polar (0001) facet can be stabilized in a reconstructed (2×2) surface by means of vacancies or adsorbates (such as the ligands).[3,14,48] The (000−1)

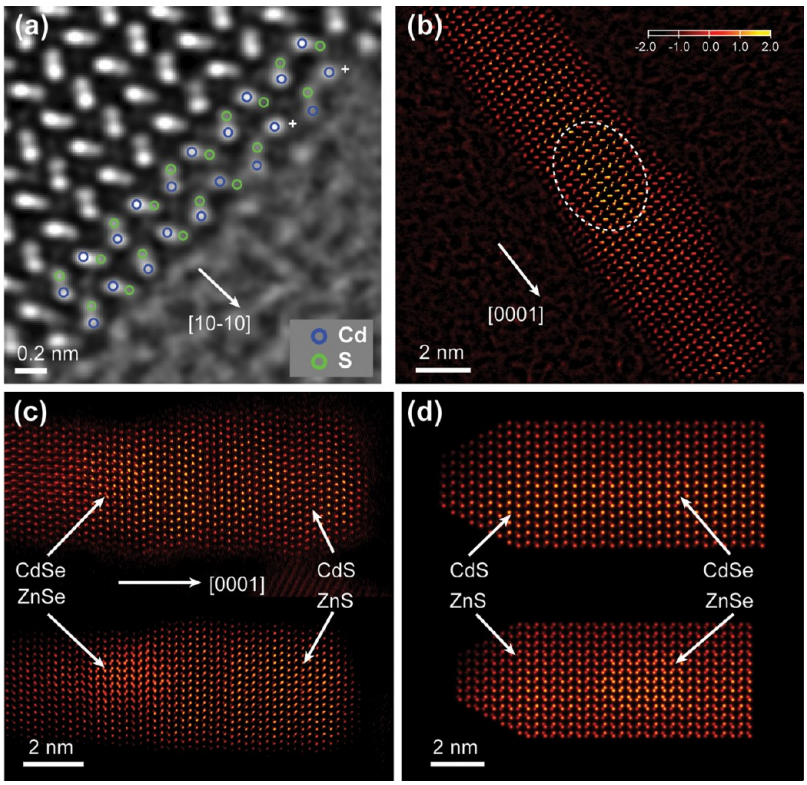

Figure 4. (a) Close-up view of a nonpolar side {10−10} edge region of the rod in Figure 2. The crosses mark columns of very dark contrast, due to missing S atoms in the columns. These surface atoms are probably removed due to beam irradiation. (b) EW phase from a ZnSe/ZnS nanorod, obtained after cation exchange reaction from CdSe/CdS rods (with color code to enhance visualization). The dumbbells from the region contoured with the dashed line clearly show a higher phase change due to the presence of Se in the core. Moreover, some cation columns in the shell show a higher phase change: they could contain Cd atoms that have not been replaced by Zn atoms. (c) Experimental HAADF-STEM image of a CdSe/CdS and a ZnSe/ZnS nanorod in [11−20] projections. The STEM analysis confirms the results from EW retrieval (the flat part of the rod is the Cd (Zn)-terminated (0001) surface). The ZnSe core is more visible in the ZnS shell than the CdSe one in CdS due to the contrast dominated by Cd in the CdSe/CdS case (contrast scaling as $\sim Z^2$). (d) Simulated linear HAADF-STEM images of the CdSe/CdS and ZnSe/ZnS nanorods, confirming the experimental result of better visibility of the ZnSe core with respect to CdSe.

facet terminated by Cd atoms is instead much less thermodynamically stable, such that the (000−1) direction is actually the faster growth direction.[3] This explains also why the core is located closer to the flat tip, ending with a (0001) facet. This picture seems common to many wurtzite nanowires and nanorods.

We recently reported the growth of octapod-shaped nanocrystals consisting of eight wurtzite CdS pods branching out from an octahedral-shaped sphalerite CdSe core.[49,50] In the octapods, four pods had a flat termination and the other four presented a sharpened tip.[47] This peculiarity in the octapods can be rationalized by considering the following: (i) in one group of four pods, each pod ends with a flat polar {0001} facet, again exposing Cd atoms with single dangling bonds; (ii) in the other group of four pods, each pod ends with multiple {10−1−1} facets, rather than with a flat {000−1} facet. The symmetry of the octapod is indeed tetrahedral rather than octahedral due to the polarity of the wurtzite structure.

Faceting of the Rods. For a comprehensive discussion of the termination beyond {0001} facets one needs to characterize the facets and their preferential termination. To this aim, we note that an integrated profile of the EW phase reveals an asymmetry, compatible with an asymmetric lateral faceting (Figure 3). We compared experimental and simulated EW phase profiles for the model in Figure 3a having three of the six nonpolar {10−10} facets as the dominant ones. To confirm this result, we show three projections from the same rod, namely, [2−1−10], [10−10], and [11−20], acquired using HAADF-STEM (Figure 3d). It is clear that the rod in the [2−1−10] and [11−20] orientations has opposite asymmetric profiles, whereas in the [10−10] orientation it has a symmetric profile, confirming the predominant {10−10} faceting (Figure 3e,f). The angles made by the atomic column projections at the tip reveal that the facets forming the tip are compatible with {10−1−1} surfaces also exposing Cd atoms (see also Figure S4 in the Supporting Information, and the blue lines of terminal Cd atoms in Figure 2d,e). These facets expose Cd atoms with a lower number of dangling bonds (one and a half per atom on average) with respect to the three of the (000−1) surface.

It is difficult to explain the dominant presence of lateral {10−10} facets by mere considerations on formation energy for the (11−20) and (10−10) nonpolar

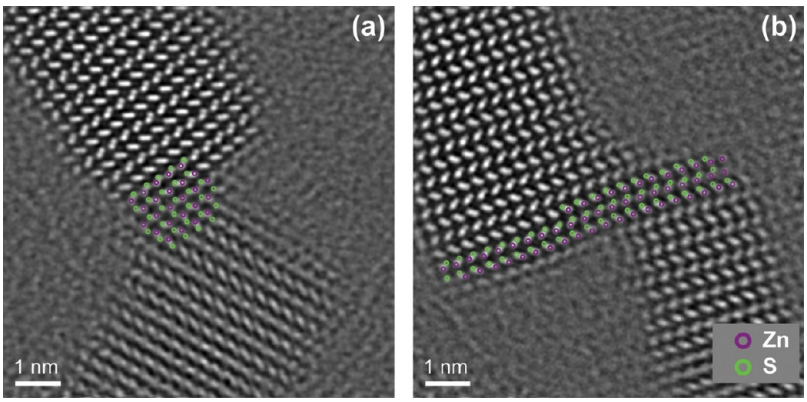

Figure 5. Some ZnSe/ZnS rods are connected by Zn−S bridges of atoms: (a) polar planes in a bottom-to-bottom junction, creating a zigzag connection between the two rods; (b) nonpolar planes connected between parallel oriented rods.

surfaces. The calculated surface energies for the two surfaces are indeed very similar, the difference being about 0.01 eV/Å^2.[12,18,51] Furthermore, the presence of edges in these quite large rods does not affect in a significant way the surface properties and perhaps only locally. Indeed, it has been shown that the surface energy of a rod facet is close to that of the corresponding clean infinite surface.[18] Different experimental[12,52] and computational studies[51] support of our findings that reveal a preference for {10−10} facets (and ascribed to a slightly shorter relaxation depth accompanied by a slightly larger residual surface polarization), while other works predict the {11−20} facets as the favored ones.[14,18]

There are other aspects that can be addresses after the Cd and S atoms have been distinguished. By careful inspection we can see that the contrast from S atoms is somewhere missing in external dumbbells, pointing to expelled atoms from the structure (Figure 4a). A possibility is that S atoms are preferentially knocked out from the structure at an incident energy of the electron beam equal to 200 kV[53] and that this process starts at the surface, where the surface S atoms are less strongly bound to the Cd atoms than the S atoms in the bulk of the nanocrystals. Indeed similar nanorods have been shown to undergo progressive etching from the external edges by continuous imaging under the electron microscope.[11]

Location of the Core. We also analyzed the ZnSe/ZnS nanorods, obtained from the CdSe/CdS rods by cation exchange. After such exchange, the rods preserved the structure of the pristine CdSe/CdS rods,[36] as can be seen in Figure 4b, where the phase after EW reconstruction is presented. Remarkably, the phase image shows in addition clear evidence of the ZnSe core buried in the ZnS shell. This is related to the effect of the heavy Se atom columns producing a stronger phase change than the S columns,[54] as expected. An alternative method to directly visualize the core with high spatial resolution is aberration-corrected HAADF-STEM. It is easier to see the core region in ZnSe/ZnS nanorods with respect to CdSe/CdS nanorods, due to the high dominant contrast produced by Cd columns in the latter system (Cd are the heaviest ones). In Figure 4c,d the HAADF-STEM images after deconvolution of the probe[55] are compared with simulations, demonstrating this point . Another interesting aspect is that also some cation columns in the ZnS shell present a stronger phase change. This is probably related to the presence of residual Cd atoms not replaced by Zn atoms. Also, by a careful look at Figure 4b it is possible to see that columns with higher contrast are more often found on the [000−1] side of the rods with respect to the core. This confirms the higher reactivity of the (000−1) surface, resulting in increasing diffusion (*i.e.*, intermixing beween the atoms from the core and the ones in the shell) toward this direction.

It is worth mentioning that in previous works CdSe (or ZnSe) cores buried inside CdS (ZnS) nanorods were visualized by strain mapping from single HRTEM images.[34,36] However, the accuracy and spatial resolution that can be obtained thanks to EW phase retrieval or HAADF-STEM are higher than with those methods.

Bridging of Atomic Columns. A remarkable difference of these ZnSe/ZnS rods with respect to their parent CdSe/CdS rods is that some of them are connected by Zn−S bridging columns (Figure 5). Two different types of connections can be found, depending on whether polar or nonpolar facets are involved. As a result, the rods can be connected parallel (nonpolar facets junction) or in a zigzag geometry (polar facets junction). This process of connection between rods can be related to reduced passivation occurring during the cation exchange process, which can lead to selective aggregation at the tips (for instance, the excess of Zn^{2+} together with S^{2-} ions redissolved in the solution can form Zn−S bridges and shell overgrowth on the lateral facets).

CONCLUSIONS

By means of EW reconstructions, we demonstrated that it is possible to unequivocally assign the Cd and S

atomic columns in HRTEM images, so that the orientation of asymmetric colloidal wurtzite nanoparticles can be fully resolved. We have found that in the [0001] direction a flat surface is formed with terminal Cd atoms, as was expected theoretically from passivation with surfactant molecules or vacancies.[3,14] In the opposite, [000−1], polar direction, a sharp tip is formed, due to oblique planes from higher index facets, exposing Cd atoms with a lower number of dangling bonds with respect to the three dangling bonds of the (000−1) Cd-terminated surface. We have verified the results determined from EW reconstruction by HAADF-STEM images. After the polar crystallographic directions of the nanorods are solved, other details can then be fully characterized, such as the faceting of the nanorods, missing atoms at the surfaces, core position, and bridging columns between nanorods. We confirmed experimentally in this way theoretical predictions on the stability of these surfaces, together with experimental speculations made on similar systems, such as tetrapods and octapods, showing similar tip and flat ends. Clearly, the approach used here can be extended to other polar nanostructures and heterostructured materials, such as ZnO or III−V nanowires. The identification and the characterization of the surfaces in nanocrystals are indeed of interest to relate structural and electronic properties in low-dimensional materials, in view of their integration in devices. The techniques for a detailed analysis of the nanostructures at the atomic level are well developed (as the EW and the HAADF-STEM shown here), and the damage to the sample during acquisition is now the factor mostly limiting the resolution. New highly sensitive detectors allowing for extremely low electron doses are then necessary to reduce the beam damage at the terminal atomic columns and to support these ultra-high-resolution techniques on nanostructures.

METHODS

Synthesis of the Nanorods. The samples investigated in this work are colloidal core/shell wurtzite CdSe/CdS nanorods (see again the sketch in Figure 1a)[34,35] and the corresponding wurtzite ZnSe/ZnS nanorods[36] derived from them *via* a sequence of two cation exchange reactions, as described by us in previous works.[36,56] The samples were dispersed in toluene, deposited on ultrathin carbon films (Ted Pella Inc.), and further annealed under vacuum at about 100 °C for 10 min, to desorb excess organic contaminants.

Experimental Conditions for NCSI Focal Series Acquisitions. HRTEM images were acquired on a JEOL JEM-2200FS microscope equipped with a 200 kV Schottky gun and a CEOS corrector in the objective lens (see the Supporting Information for details regarding the imaging conditions). The possibility of tuning the spherical aberration permits to find a compromise between high transfer amounts of higher frequencies (*e.g.*, that needed to see the dumbbells in the wurtzite CdSe/CdS nanorods) up to the maximum frequency g_{max} (information limit) and a reduced delocalization. Following the method explained by Urban *et al.*,[43] one ends up with the following formulas for the defocus *C*1 and the spherical aberration *C*3:

$$C1 = \frac{16}{9}\frac{1}{\lambda g_{max}^2} \quad C3 = -\frac{64}{27}\frac{1}{\lambda^3 g_{max}^4} \qquad (1)$$

where λ is the electron wavelength and $g_{max} = 8.5\ nm^{-1}$ is the measured information limit of the instrument. The chosen signs are the ones corresponding to negative *C*3 imaging (NCSI), in which atoms produce bright contrast.[43] The images were acquired at 2048 × 2048 resolution with a pixel corresponding to 0.012 nm, so as to sample the Nyquist frequency $1/2g_{max}$ accurately. In this way the point spread function of the CCD detector could be neglected. For image simulations, we used the "multislice" method[57] within the software STEM_CELL.[58,59]

Details of the Exit Wave Analysis. In order to obtain interpretable information from EW reconstruction, we use the simple channeling model.[44] The intensity on the maxima can be written

$$\psi(\mathbf{r}, z) = 1 + C_{1s}\varphi_{1s}(\mathbf{r} - \mathbf{r}_i)\left[\exp\left(-i\pi\frac{E_{1s}}{E_0}\frac{z}{\lambda}\right) - 1\right] \qquad (2)$$

with E_{1s} and $C_{1s}\phi_{1s}(\mathbf{r} - \mathbf{r}_i)$ the eigenvalue and eigenvector of the dominant 1s state of the atom in the column, E_0 is the incident energy, and z is the depth. Equation 2 can be rewritten, by substituting $A(\mathbf{r} - \mathbf{r}_i) = C_{1s}\phi_{1s}(\mathbf{r} - \mathbf{r}_i)$ with

$$\psi(\mathbf{r}, z) = 1 - A(\mathbf{r} - \mathbf{r}_i) + A(\mathbf{r} - \mathbf{r}_i)\exp\left(-i\pi\frac{E_{1s}}{E_0}\frac{z}{\lambda}\right) \qquad (3)$$

This in the Argand−Gauss plane is a circle translated by the real amount $1 - A$.

The *exit wave* (*i.e.*, the wave function at the exit plane of the object) was retrieved using the iterative wave function restoration (IWFR) software from HREM Research Inc. (Japan), using sets of 20 images, after carefully measuring the defocus values by fitting the diffractogram of the amorphous region (Figure S2a). In the reconstructed exit waves the Cd (*i.e.*, most intense) peak positions have been fitted within STEM_CELL and an Argand−Gauss plot for each maximum has been plotted. The experimental plot is shown in Figure S2b. The data have been fitted with a circle according to eq 3, finding a center at $z_c = 0.88 + i0.29$. This complex constant has been subtracted from the data, obtaining a phase that is now directly proportional to Zt, where Z is the atomic number and t is the specimen thickness.

HAADF-STEM Images and Simulations. HAADF-STEM images were acquired on a FEI Titan^3 50-80 microscope equipped with both image and probe correctors and working at 120 or 300 kV. The acquisitions conditions were beam convergence 21.4 mrad, probe nominal size 0.08 nm, and HAADF inner collection semiangle approximately 30 mrad. To simulate the contrast in the images, we used the linear model proposed by Kirkland[57] and implemented in STEM_CELL. Intensity is calculated as:

$$I(\mathbf{r}) = P^2 \otimes V^2 \otimes S \qquad (4)$$

where P^2 is the probe, V^2 is the squared potential, and S is a Gaussian ($\sigma = 0.05$ nm) to account for the finite source size.

Conflict of Interest: The authors declare no competing financial interest.

Supporting Information Available: Conditions of HRTEM and HAADF-STEM imaging with aberration correction with details on image simulations and exit wave extraction from HRTEM; further HRTEM images of the structure of the nanorods and the original seeds. This material is available free of charge *via* the Internet at http://pubs.acs.org.

Acknowledgment. The authors gratefully acknowledge funding from the European Research Council under grant number 240111 (NANO-ARCH) and the financial support from

the Flemish Hercules 3 Programme for large infrastructures. G.B. and V.G. thank E. Rotunno for his help with STEM_CELL and IWFR.

REFERENCES AND NOTES

1. Fultz, B.; Howe, J. *Transmission Electron Microscopy and Dif fractometry of Materials*, 3rd ed.; Springer: Berlin, 2009.
2. Spiecker, E. Determination of Crystal Polarity from Bend Contours in Transmission Electron Microscope Images. *Ultramicroscopy* **2002**, *92*, 111–132.
3. Rempel, J. Y.; Trout, B. L.; Bawendi, M. G.; Jensen, K. F. Properties of the CdSe(0001), (000−1), and (11−20) Single Crystal Surfaces: Relaxation, Reconstruction, and Adatom and Admolecule Adsorption. *J. Phys. Chem. B* **2005**, *109*, 19320–19328.
4. Brillson, L. J.; Lu, Y. ZnO Schottky Barriers and Ohmic Contacts. *J. Appl. Phys.* **2011**, *109*, 121301–33.
5. Kuykendall, T.; Pauzauskie, P. J.; Zhang, Y.; Goldberger, J.; Sirbuly, D.; Denlinger, J.; Yang, P. Crystallographic Alignment of High-Density Gallium Nitride Nanowire Arrays. *Nat. Mater.* **2004**, *3*, 524–528.
6. Mitate, T.; Sonoda, Y.; Kuwano, N. Polarity Determination of Wurtzite and Zincblende Structures by TEM. *Phys. Status Solidi A* **2002**, *192*, 383–388.
7. Williams, J. R.; Kobata, M.; Pis, I.; Ikenaga, E.; Sugiyama, T.; Kobayashi, K.; Ohashi, N. Polarity Determination of Wurtzite-Type Crystals Using Hard X-Ray Photoelectron Diffraction. *Surf. Sci.* **2011**, *605*, 1336–1340.
8. Shiang, J. J.; Kadavanich, A. V.; Grubbs, R. K.; Alivisatos, A. P. Symmetry of Annealed Wurtzite CdSe Nanocrystals: Assignment to the $C3_v$ Point Group. *J. Phys. Chem.* **1995**, *99*, 17417–17422.
9. Fang, C.; van Huis, M. A.; Vanmaekelbergh, D. I.; Zandbergen, H. W. Energetics of Polar and Nonpolar Facets of PbSe Nanocrystals from Theory and Experiment. *ACS Nano* **2009**, *4*, 211–218.
10. Figuerola, A.; Huis, M. v.; Zanella, M.; Genovese, A.; Marras, S.; Falqui, A.; Zandbergen, H. W.; Cingolani, R.; Manna, L. Epitaxial CdSe-Au Nanocrystal Heterostructures by Thermal Annealing. *Nano Lett.* **2010**, *10*, 3028–3036.
11. van Huis, M. A.; Figuerola, A.; Fang, C.; Béché, A.; Zandbergen, H. W.; Manna, L. Chemical Transformation of Au-Tipped CdS Nanorods into AuS/Cd Core/Shell Particles by Electron Beam Irradiation. *Nano Lett.* **2011**, *11*, 4555–4561.
12. Liu, W.; Wang, N.; Wang, R.; Kumar, S.; Duesberg, G. S.; Zhang, H.; Sun, K. Atom-Resolved Evidence of Anisotropic Growth in ZnS Nanotetrapods. *Nano Lett.* **2011**, *11*, 2983–2988.
13. Manna, L.; Scher, E. C.; Alivisatos, A. P. Synthesis of Soluble and Processable Rod-, Arrow-, Teardrop-, and Tetrapod-Shaped CdSe Nanocrystals. *J. Am. Chem. Soc.* **2000**, *122*, 12700–12706.
14. Manna, L.; Wang; Cingolani, R.; Alivisatos, A. P. First-Principles Modeling of Unpassivated and Surfactant-Passivated Bulk Facets of Wurtzite CdSe: A Model System for Studying the Anisotropic Growth of CdSe Nanocrystals. *J. Phys. Chem. B* **2005**, *109*, 6183–6192.
15. Zhang, H.; Ha, D.-H.; Hovden, R.; Kourkoutis, L. F.; Robinson, R. D. Controlled Synthesis of Uniform Cobalt Phosphide Hyperbranched Nanocrystals Using Tri-*n*-octylphosphine Oxide as a Phosphorus Source. *Nano Lett.* **2011**, *11*, 188–197.
16. Ithurria, S.; Tessier, M. D.; Mahler, B.; Lobo, R.; Dubertret, B.; Efros, A. Colloidal Nanoplatelets with Two-Dimensional Electronic Structure. *Nat. Mater.* **2011**, *10*, 936–941.
17. Schliehe, C.; Juarez, B. H.; Pelletier, M.; Jander, S.; Greshnykh, D.; Nagel, M.; Meyer, A.; Foerster, S.; Kornowski, A.; Klinke, C.; *et al.* Ultrathin PbS Sheets by Two-Dimensional Oriented Attachment. *Science* **2010**, *329*, 550–553.
18. Leitsmann, R.; Bechstedt, F. Surface Influence on Stability and Structure of Hexagon-Shaped III-V Semiconductor Nanorods. *J. Appl. Phys.* **2007**, *102*, 063528–8.
19. Kopping, J. T.; Patten, T. E. Identification of Acidic Phosphorus-Containing Ligands Involved in the Surface Chemistry of CdSe Nanoparticles Prepared in Tri-*n*-octylphosphine Oxide Solvents. *J. Am. Chem. Soc.* **2008**, *130*, 5689–5698.
20. Owen, J. S.; Park, J.; Trudeau, P.-E.; Alivisatos, A. P. Reaction Chemistry and Ligand Exchange at Cadmium-Selenide Nanocrystal Surfaces. *J. Am. Chem. Soc.* **2008**, *130*, 12279–12281.
21. Cooper, J. K.; Franco, A. M.; Gul, S.; Corrado, C.; Zhang, J. Z. Characterization of Primary Amine Capped CdSe, ZnSe, and ZnS Quantum Dots by FT-IR: Determination of Surface Bonding Interaction and Identification of Selective Desorption. *Langmuir* **2011**, *27*, 8486–8493.
22. Puzder, A.; Williamson, A. J.; Zaitseva, N.; Galli, G.; Manna, L.; Alivisatos, A. P. The Effect of Organic Ligand Binding on the Growth of CdSe Nanoparticles Probed by Ab Initio Calculations. *Nano Lett.* **2004**, *4*, 2361–2365.
23. Rempel, J. Y.; Trout, B. L.; Bawendi, M. G.; Jensen, K. F. Density Functional Theory Study of Ligand Binding on CdSe (0001), (000−1), and (11−20) Single Crystal Relaxed and Reconstructed Surfaces: Implications for Nanocrystalline Growth. *J. Phys. Chem. B* **2006**, *110*, 18007–18016.
24. Luo, Y.; Wang, L.-W. Electronic Structures of the CdSe/CdS Core-Shell Nanorods. *ACS Nano* **2009**, *4*, 91–98.
25. Gomes, R.; Hassinen, A.; Szczygiel, A.; Zhao, Q.; Vantomme, A.; Martins, J. C.; Hens, Z. Binding of Phosphonic Acids to CdSe Quantum Dots: A Solution NMR Study. *J. Phys. Chem. Lett.* **2011**, *2*, 145–152.
26. Bealing, C. R.; Baumgardner, W. J.; Choi, J. J.; Hanrath, T.; Hennig, R. G. Predicting Nanocrystal Shape through Consideration of Surface-Ligand Interactions. *ACS Nano* **2012**, *6*, 2118–2127.
27. Kudera, S.; Carbone, L.; Casula, M. F.; Cingolani, R.; Falqui, A.; Snoeck, E.; Parak, W. J.; Manna, L. Selective Growth of PbSe on One or Both Tips of Colloidal Semiconductor Nanorods. *Nano Lett.* **2005**, *5*, 445–449.
28. Mokari, T.; Sztrum, C. G.; Salant, A.; Rabani, E.; Banin, U. Formation of Asymmetric One-Sided Metal-Tipped Semiconductor Nanocrystal Dots and Rods. *Nat. Mater.* **2005**, *4*, 855–863.
29. Habas, S. E.; Yang, P.; Mokari, T. Selective Growth of Metal and Binary Metal Tips on CdS Nanorods. *J. Am. Chem. Soc.* **2008**, *130*, 3294–3295.
30. Mokari, T.; Rothenberg, E.; Popov, I.; Costi, R.; Banin, U. Selective Growth of Metal Tips onto Semiconductor Quantum Rods and Tetrapods. *Science* **2004**, *304*, 1787–1790.
31. O'Sullivan, C.; Gunning, R. D.; Barrett, C. A.; Singh, A.; Ryan, K. M. Size Controlled Gold Tip Growth Onto II-VI Nanorods. *J. Mater. Chem.* **2010**, *20*, 7875–7880.
32. O'Sullivan, C.; Gunning, R. D.; Sanyal, A.; Barrett, C. A.; Geaney, H.; Laffir, F. R.; Ahmed, S.; Ryan, K. M. Spontaneous Room Temperature Elongation of CdS and Ag_2S Nanorods via Oriented Attachment. *J. Am. Chem. Soc.* **2009**, *131*, 12250–12257.
33. Talapin, D. V.; Koeppe, R.; Götzinger, S.; Kornowski, A.; Lupton, J. M.; Rogach, A. L.; Benson, O.; Feldmann, J.; Weller, H. Highly Emissive Colloidal CdSe/CdS Heterostructures of Mixed Dimensionality. *Nano Lett.* **2003**, *3*, 1677–1681.
34. Carbone, L.; Nobile, C.; De Giorgi, M.; Sala, F. D.; Morello, G.; Pompa, P.; Hytch, M.; Snoeck, E.; Fiore, A.; Franchini, I. R.; *et al.* Synthesis and Micrometer-Scale Assembly of Colloidal CdSe/CdS Nanorods Prepared by a Seeded Growth Approach. *Nano Lett.* **2007**, *7*, 2942–2950.
35. Talapin, D. V.; Nelson, J. H.; Shevchenko, E. V.; Aloni, S.; Sadtler, B.; Alivisatos, A. P. Seeded Growth of Highly Luminescent CdSe/CdS Nanoheterostructures with Rod and Tetrapod Morphologies. *Nano Lett.* **2007**, *7*, 2951–2959.
36. Li, H.; Brescia, R.; Krahne, R.; Bertoni, G.; Alcocer, M. J. P.; D'Andrea, C.; Scotognella, F.; Tassone, F.; Zanella, M.; De Giorgi, M.; *et al.* Blue-UV-Emitting ZnSe(Dot)/ZnS(Rod) Core/Shell Nanocrystals Prepared from CdSe/CdS Nanocrystals by Sequential Cation Exchange. *ACS Nano* **2012**, *6*, 1637–1647.
37. Jain, P. K.; Amirav, L.; Aloni, S.; Alivisatos, A. P. Nanoheterostructure Cation Exchange: Anionic Framework Conservation. *J. Am. Chem. Soc.* **2010**, *132*, 9997–9999.
38. McBride, J.; Treadway, J.; Feldman, L. C.; Pennycook, S. J.; Rosenthal, S. J. Structural Basis for Near Unity Quantum Yield Core/Shell Nanostructures. *Nano Lett.* **2006**, *6*, 1496–1501.

39. Rosenthal, S. J.; McBride, J.; Pennycook, S. J.; Feldman, L. C. Synthesis, Surface Studies, Composition and Structural Characterization of CdSe, Core/Shell and Biologically Active Nanocrystals. *Surf. Sci. Rep.* **2007**, *62*, 111–157.
40. McBride, J. R.; Kippeny, T. C.; Pennycook, S. J.; Rosenthal, S. J. Aberration-Corrected Z-Contrast Scanning Transmission Electron Microscopy of CdSe Nanocrystals. *Nano Lett.* **2004**, *4*, 1279–1283.
41. Mkhoyan, K. A.; Batson, P. E.; Cha, J.; Schaff, W. J.; Silcox, J. Direct Determination of Local Lattice Polarity in Crystals. *Science* **2006**, *312*, 1354.
42. Lentzen, M.; Jahnen, B.; Jia, C. L.; Thust, A.; Tillmann, K.; Urban, K. High-Resolution Imaging with an Aberration-Corrected Transmission Electron Microscope. *Ultramicroscopy* **2002**, *92*, 233–242.
43. Urban, K. W.; Jia, C.-L.; Houben, L.; Lentzen, M.; Mi, S.-B.; Tillmann, K. Negative Spherical Aberration Ultrahigh-Resolution Imaging in Corrected Transmission Electron Microscopy. *Philos. Trans. R. Soc. A* **2009**, *367*, 3735–3753.
44. Van Dyck, D.; Op De Beeck, M. A Simple Intuitive Theory for Electron Diffraction. *Ultramicroscopy* **1996**, *64*, 99–107.
45. Pennycook, S. J. Z-contrast Stem for Materials Science. *Ultramicroscopy* **1989**, *30*, 58–69.
46. Tillmann, K.; Thust, A.; Urban, K. Spherical Aberration Correction in Tandem with Exit-Plane Wave Function Reconstruction: Interlocking Tools for the Atomic Scale Imaging of Lattice Defects in GaAs. *Microsc. Microanal.* **2004**, *10*, 185–198.
47. Brescia, R.; Miszta, K.; Dorfs, D.; Manna, L.; Bertoni, G. Birth and Growth of Octapod-Shaped Colloidal Nanocrystals Studied by Electron Tomography. *J. Phys. Chem. C* **2011**, *115*, 20128–20133.
48. Meyer, B.; Marx, D. Density-Functional Study of the Structure and Stability of ZnO Surfaces. *Phys. Rev. B* **2003**, *67*, 035403–11.
49. Deka, S.; Miszta, K.; Dorfs, D.; Genovese, A.; Bertoni, G.; Manna, L. Octapod-Shaped Colloidal Nanocrystals of Cadmium Chalcogenides via "One-Pot" Cation Exchange and Seeded Growth. *Nano Lett.* **2010**, *10*, 3770–3776.
50. Miszta, K.; de Graaf, J.; Bertoni, G.; Dorfs, D.; Brescia, R.; Marras, S.; Ceseracciu, L.; Cingolani, R.; van Roij, R.; Dijkstra, M.; *et al.* Hierarchical Self-Assembly of Suspended Branched Colloidal Nanocrystals into Superlattice Structures. *Nat. Mater.* **2011**, *10*, 872–876.
51. Brandino, G. P.; Cicero, G.; Bonferroni, B.; Ferretti, A.; Calzolari, A.; Bertoni, C. M.; Catellani, A. Polarization Properties of (1−100) and (11−20) SiC Surfaces from First Principles. *Phys. Rev. B* **2007**, *76*, 085322–9.
52. Diebold, U.; Koplitz, L. V.; Dulub, O. Atomic-Scale Properties of Low-Index ZnO Surfaces. *Appl. Surf. Sci.* **2004**, *237*, 336–342.
53. Hamid, S. A. Identification of the Displaced Atomic Species for Binary Semiconducting Compounds. *J. Phys. C: Solid State Phys.* **1971**, *4*, 2635–2636.
54. Bals, S.; Casavola, M.; van Huis, M. A.; Van Aert, S.; Batenburg, K. J.; Van Tendeloo, G.; Vanmaekelbergh, D. I. Three-Dimensional Atomic Imaging of Colloidal Core-Shell Nanocrystals. *Nano Lett.* **2011**, *11*, 3420–3424.
55. Grillo, V. Advances in STEM-CELL. A Free Software for TEM and STEM Analysis and Simulations: Probe Deconvolution in STEM-HAADF. *Microsc. Microanal.* **2011**, *17*, 1292–1293.
56. Li, H.; Zanella, M.; Genovese, A.; Povia, M.; Falqui, A.; Giannini, C.; Manna, L. Sequential Cation Exchange in Nanocrystals: Preservation of Crystal Phase and Formation of Metastable Phases. *Nano Lett.* **2011**, *11*, 4964–4970.
57. Kirkland, E. J. *Advanced Computing in Electron Microscopy*; Springer: New York, 2010.
58. D'Addato, S.; Grillo, V.; Altieri, S.; Tondi, R.; Valeri, S.; Frabboni, S. Structure and Stability of Nickel/Nickel Oxide Core-Shell Nanoparticles. *J. Phys.: Condens. Matter* **2011**, *23*, 175003–7.
59. Grillo, V. *Stemcell: A Software Project*; 2009, http://tem-s3.nano.cnr.it/stemcell.htm.